ARTICLE OPEN

Check for updates

Orbital-selective Mott and Peierls transition in H_xVO_2

Soyeun Kim[1,2], Steffen Backes[3,4,5], Hyojin Yoon[6], Woojin Kim[1,2], Changhee Sohn[7], Junwoo Son[6], Silke Biermann[3,4,5,8], Tae Won Noh[1,2]✉ and Se Young Park[1,2,9]✉

Materials displaying metal-insulator transitions (MITs) as a function of external parameters such as temperature, pressure, or composition are most intriguing from the fundamental point of view and also hold high promise for applications. Vanadium dioxide (VO_2) is one of the most prominent examples of MIT having prospective applications ranging from intelligent coatings, infrared sensing, or imaging, to Mott memory and neuromorphic devices. The key aspects conditioning possible applications are the controllability and reversibility of the transition. Here we present an intriguing MIT in hydrogenated vanadium dioxide, H_xVO_2. The transition relies on an increase of the electron occupancy through hydrogenation on the transition metal vanadium, driving the system insulating by a hybrid of two distinct MIT mechanisms. The insulating phase observed in HVO_2 with a nominal d^2 electronic configuration contrasts with other rutile d^2 systems, most of which are metallic. Using spectroscopic tools and state-of-the-art many-body electronic structure calculations, our investigation reveals a correlation-enhanced Peierls and a Mott transition taking place in an orbital-selective manner cooperate to stabilize an insulating phase. The identification of the hybrid mechanism for MIT controlled by hydrogenation opens the way to radically design strategies for future correlated oxide devices by controlling phase reversibly while maintaining high crystallinity.

npj Quantum Materials (2022)7:95 ; https://doi.org/10.1038/s41535-022-00505-y

INTRODUCTION

Identifying low energy degrees of freedom and their intricate interplay in correlated electron materials is essential to understanding their physical properties. For metal-to-insulator-transitions (MIT) in particular, strong electronic correlations often play a crucial role in the charge localization of systems with non-trivial band fillings. In these systems, the MIT often occurs with either formation of orderings or enhancement of the pre-existing ones, resulting from an intricate interrelationship of lattice, charge, orbital, and spin degrees of freedom. The MITs accompanied by such an emergence or enhancement of orderings have been reported in many transition metal oxides[1,2].

Vanadium dioxide (VO_2) is one of the most prominent examples of the correlation-driven MIT that has excited the solid-state community for decades[3–6]. VO_2 undergoes MIT around $T_{MIT} \sim 340$ K[7] with a structural transition from a rutile to a monoclinic phase (M1), involving the formation of V–V dimers. The insulating state can be understood as a combined effect of V–V dimerization and the on-site Coulomb interaction. The former induces a bonding-antibonding splitting within the a_{1g} orbitals with a strong bonding along the dimer direction[8]. The latter opens a gap by enhancing the bonding-antibonding splitting, resulting in a spin-singlet state in the filled bonding band[9–12].

Recently, the electronic transport and lattice structure of hydrogenated VO_2 (H_xVO_2) have been investigated[13–18]. H_xVO_2 shows successive phase transitions as a function of hydrogen content x at room temperature: an insulator to metal transition followed by the reentrance of the insulating phase. At low H-content, it shows a bad metallic behavior with a resistivity exceeding the Mott–Ioffe–Regel limit[19,20], implying strong electron–electron interactions[21]. Electronic and optical properties in the metallic phase at low hydrogenation are similar to the oxygen vacant $VO_{2-\delta}$[22]. As H-doping increases, a structural transition involving dimerization of V-cations occurs[18] [Fig. 1a], accompanied by a MIT in the electronic transport. The insulating phase is maintained up to the fully hydrogenated limit (HVO_2)[23,24]. Since the inserted hydrogen is attached to oxygen atoms and hybridizes mainly with O-p states away from the Fermi energy, the primary role of the hydrogenation is changing the V-d occupancy, consistent with density functional theory (DFT) calculations[23,24]. Thus, the doping-induced change in the valence suggests the presence of a filling-controlled MIT around the V-d^2-filling, which is in clear contrast to other d^2-filling rutile-based compounds such as CrO_2, MoO_2, and WO_2 showing a low-T metallic phase[25–27].

Identification of this newly discovered MIT mechanism requires orbital-sensitive measurements to probe the orbital reconstructions associated with the MIT. Moreover, computational methods incorporating both intra- and inter-site correlations need to be employed to correctly capture the essential many-body effects, such as cluster dynamical mean-field theory (CDMFT), which successfully captures the MIT in VO_2[11]. We investigate the mechanism of the MIT by polarization-dependent spectroscopic ellipsometry and X-ray absorption (XAS) measurements, elucidating the orbital-dependent spectral modifications in the insulating phase. The orbital reconstructions accompanied by the MIT are theoretically investigated considering both on-site and inter-site correlation using Δ+DMFT scheme, which successfully capture the orbital structures observed in the experiments. From our analysis, we will show that the MIT is driven by a simultaneous Mott and Peierls transition depending on the orbital character. Our

[1]Center for Correlated Electron Systems, Institute for Basic Science (IBS), Seoul 08826, Korea. [2]Department of Physics and Astronomy, Seoul National University (SNU), Seoul 08826, Korea. [3]CPHT, CNRS, Ecole Polytechnique, Institut Polytechnique de Paris, 91128 Palaiseau, France. [4]Collège de France, 11 place Marcelin Berthelot, 75005 Paris, France. [5]European Theoretical Spectroscopy Facility, 91128 Palaiseau, France. [6]Department of Materials Science and Engineering, Pohang University of Science and Technology (POSTECH), Pohang 37673, Korea. [7]Department of Physics, Ulsan National Institute of Science and Technology (UNIST), Ulsan 44919, Korea. [8]Department of Physics, Division of Mathematical Physics, Lund University, Professorsgatan 1, 22363 Lund, Sweden. [9]Department of Physics and Origin of Matter and Evolution of Galaxies (OMEG) Institute, Soongsil University, Seoul 06978, Korea. ✉email: twnoh@snu.ac.kr; sp2829@ssu.ac.kr

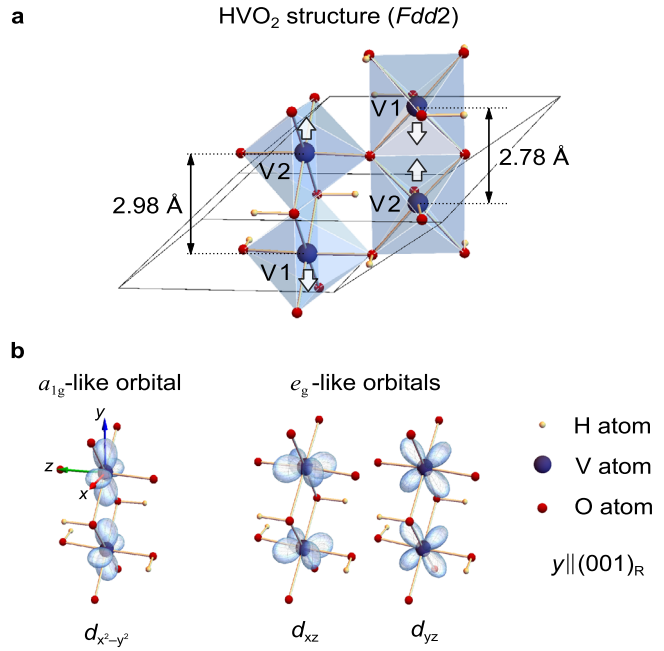

Fig. 1 Atomic structure and frontier orbitals of HVO_2. a The primitive unit cell of insulating HVO_2 in orthorhombic structure (space group *Fdd*2). Similar to VO_6, the octahedra are edge-sharing in the $(001)_R$ direction and corner-sharing in $(100)_R/(010)_R$ directions, forming chain-like structures with small octahedral rotations. Two inequivalent V sites with four and two hydrogen atoms attached to the VO_6 octahedron are defined as V1 and V2, respectively. The V–V bond lengths are 2.98 and 2.78 Å, which are comparable to experimental values of monoclinic VO_2 3.10 and 2.77 Å[9,42]. **b** Definition of vanadium $d_{x^2-y^2}$ (a_{1g}-like) and d_{xz}/d_{yz} (e_g^π-like) orbitals in this work. The *y*-axis is set parallel to V-chain direction $(001)_R$.

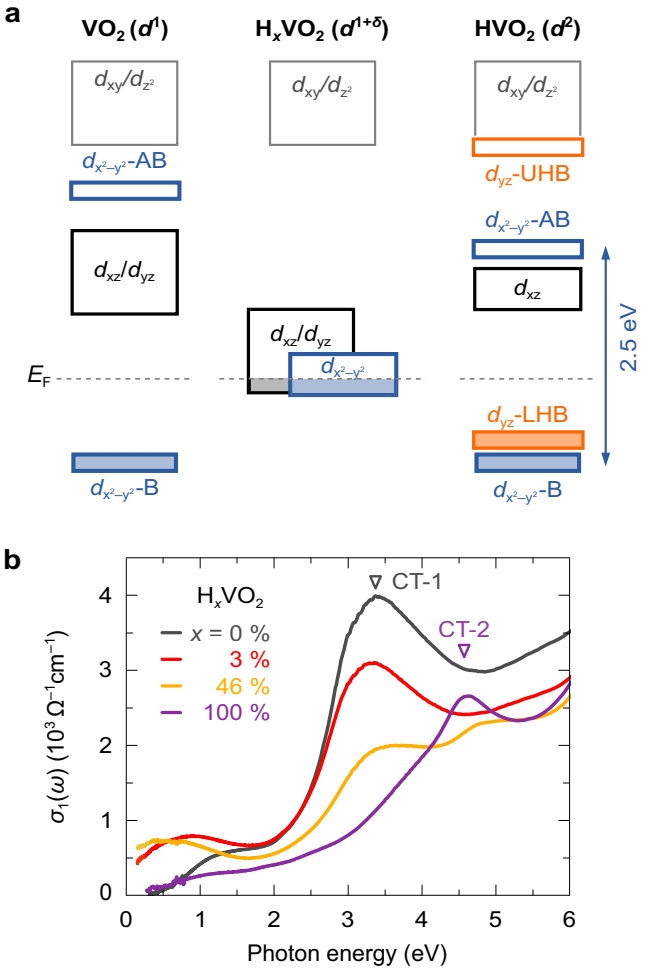

Fig. 2 Orbital structures and optical conductivity of H_xVO_2. a Schematic energy band diagrams for the insulating VO_2, metallic H_xVO_2, and insulating HVO_2 near Fermi level. **b** Real part of the optical conductivity of H_xVO_2 thin film on Al_2O_3 (0001) substrate measured at room temperature. CT, charge transfer; B, bonding; AB, antibonding; UHB, upper-Hubbard band; LHB, lower-Hubbard band.

experimental data provides the spectral information of H_xVO_2 essential for the characterization of electronic structures across the MIT and to the best of our knowledge this is the first proposal of the MIT mechanism involving Mott and Peierls physics with orbital-dependent way, which has not been reported in rutile systems. We expect that the hybrid mechanism along with the continuous control of hydrogenation can provide ways control phase of the matter, which is important to utilize the vanadium-based oxides as various applications[27–31] such as hydrogen storage and high-performance smart windows[24,32–34].

RESULTS AND DISCUSSION

Effects of the hydrogenation

Figure 2a summarizes our main findings by comparing schematic orbital structures of undoped, partially hydrogenated, and fully hydrogenated H_xVO_2. Since the average occupancy of V-*d* orbitals is expected to be in between one and two electrons per V, the low-lying frontier orbitals of H_xVO_2 are a_{1g}- and e_g^π-like orbitals, with lobes extended along and perpendicular to the dimer direction, respectively, as presented in Fig. 1b. Starting from the insulating VO_2 system involving the correlation-enhanced bonding-antibonding splitting of $d_{x^2-y^2}$ (a_{1g}) (left panel), the introduction of a small amount of hydrogen leads to an insulator to metal transition as the added electrons occupy the partially occupied e_g^π orbitals (middle panel), consistent with other electron-doped VO_2 systems[17,27,35].

As the electron occupancy reaches 2 electrons per vanadium in the fully hydrogenated HVO_2, a MIT occurs with a structural transition involving the dimerization of V atoms [Fig. 1a]. Just as the filling the bonding state of $d_{x^2-y^2}$ opens a gap in dimerized VO_2 (left panel), it is strongly suggested that the similar splitting of a_{1g} orbitals is also present in HVO_2 as the dimerization occurs simultaneously with the MIT[36,37]. With a *d*-occupancy of 2 electrons per V around $x = 100\%$, an additional orbital splitting is expected to induce the band gap. As in Fig. 2, the MIT occurs in which d_{yz} orbitals split to the lower and upper Hubbard bands by a Mott-transition with an orbital ordering between d_{xz} and d_{yz} orbitals, pushing up the energy of d_{xz} orbital relative to d_{yz}. Here, the role of electron correlations is essential, which boosts the orbital ordering and, at the same time, opens a gap by splitting the d_{yz} bands.

To understand the evolution of the electronic structure in HVO_2, we examine the structural changes developed by hydrogenation. X-ray and neutron diffraction studies verified the lattice structure of H_xVO_2 and identified orthorhombic structure (space group *Fdd*2(43)) for highly hydrogenated and insulating phase[18]. The structural characterization of our epitaxial films is published elsewhere[37]. As illustrated in Fig. 1a, it has four V atoms in the primitive unit cell. We note that HVO_2 has substantial dimerization along the V-chain with long (short) bonds between vanadium sites with (without) H attached to the bridging oxygens.

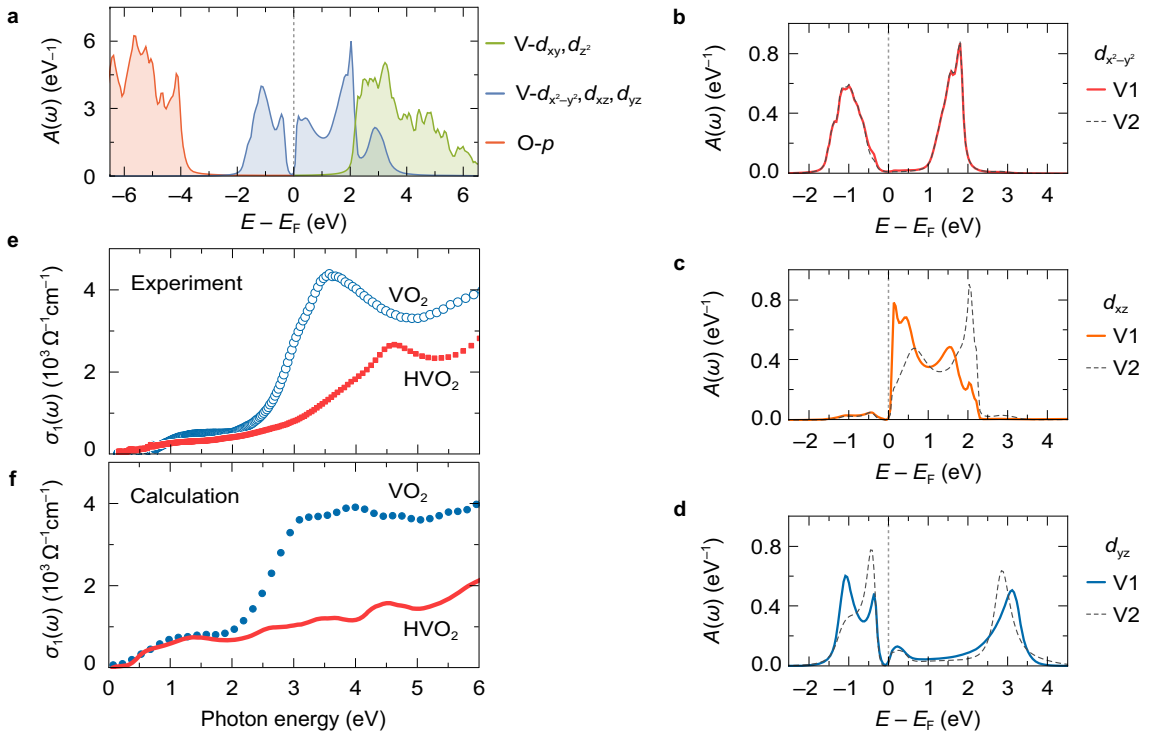

Fig. 3 Δ+DMFT calculation of the insulating HVO_2. a The spectral function $A(\omega)$ of O-p (red), V-da_{1g}/e_g^{π}-like (blue), and V-d e_g^{σ}-like (green) orbital dominated states. **b–d** Orbital decomposed $A(\omega)$ of **b** $d_{x^2-y^2}$, **c** d_{xz}, and **d** d_{yz} orbitals. The inequivalent V1 and V2 atoms are indicated by solid and dashed lines, respectively. **e** Experimental optical conductivity $\sigma_1(\omega)$ of VO_2 measured at 180 K (empty circles) and HVO_2 at 300 K (filled squares) grown on Al_2O_3 (0001) substrate. As the in-plane lattice directions of the sample are not aligned within the beam spot, the optical anisotropy was undetected. **f** Calculated $\sigma_1(\omega)$ of the Δ+DMFT method for insulating VO_2 (dotted line) and HVO_2 (solid line). The spectra for the two polarizations, $E \parallel (001)_R$ and $E \parallel (010)_R$, is averaged for direct comparison to the experiment.

Electronic structures and optical conductivity

A pronounced insulator-to-metal transition and reentrance to the insulating phase of H_xVO_2 at room temperature are well-exhibited in the real part of the optical conductivity $\sigma_1(\omega)$ in Fig. 2b. The subsequent transitions observed by increasing x are consistent with transport measurements[23,24]. At $x = 0\%$, the overall peak structure of our film is in good agreement with previous reports on monoclinic VO_2[38]. We can observe an optical gap between filled a_{1g} and e_g^{π} orbitals. The low-intensity peaks near 1.2 and 3 eV are mainly attributed to transitions within V-d orbitals, shown schematically in Fig. 2a. A peak near 3.5 eV marked as CT-1 is the charge transfer peak and corresponds to the excitation from O-p to V-d derived bands[39,40].

At $x = 3\%$, the optical gap is closed, while the charge transfer peak is almost fully maintained except for a decrease in peak height. We find the gap reopening at $x = 100\%$, reentering the insulating phase. We note here that the composition x is estimated by optical and diffraction characteristics of H_xVO_2 (see "Methods" and Fig. S2 in the Supplementary Information), which may deviate from exact chemical stoichiometry. The charge transfer peak is shifted higher in energy by 1.3 eV (marked as CT-2) with largely reduced spectral weight over the measured frequency range. At intermediate H-content of $x = 46\%$, $\sigma_1(\omega)$ shows two charge transfer peaks. At the same doping, the coexistence of two XRD peaks that correspond to the $(100)_R$ lattice of low and high H-compositions ($x = 3\%$ and 100%) are observed (see Fig. S2b in the Supplementary Information for details).

We now investigate the electronic structure of the insulating O2 phase in the fully hydrogenated limit (HVO_2), including the effect of strong local Coulomb interactions on the V-d orbitals. For this, we employ a Δ+DMFT approach, where we project the DFT Hamiltonian onto localized a_{1g}- and e_g^{π}-like Wannier orbitals for the two inequivalent V atoms in the unit cell as in Fig. 1b. In the reduced model, the on-site correlations of d_{xz} and d_{yz} orbitals are treated by DMFT utilizing a continuous-time Quantum Monte Carlo impurity solver. Our approximation properly respects the fact that the intra- and inter-dimer hopping energies of d_{xz} and d_{yz} orbitals are similar in magnitude and can be considered a local problem, adequately described in a DMFT approach. On the other hand, the inter-site correlations originating from the dimer-forming $d_{x^2-y^2}$ orbitals are approximated by a static (frequency-independent) dimer-like self-energy of the form of an inter-site orbital-dependent potential Δ as described in ref. [41]. This approach effectively captures the correlation-enhanced bonding-antibonding splitting of e_g^{π} orbitals. Such a static treatment of the inter-site correlations has been previously employed in pure VO_2 by a LDA+Δ correction[41].

Figure 3a presents the orbital-projected spectral function for HVO_2 calculated within the Δ+DMFT method. We find a Mott-insulating phase with a gap at the Fermi energy (E_F), consistent with our optical spectra [Fig. 2b] and previous transport experiments[23,36,42]. The O-p derived bands are −4 eV below the E_F which is roughly 1.5 eV lower than those of metallic H_xVO_2 and of pure VO_2[26], which is consistent with the blue shift of the charge transfer peak observed in our optical spectra [CT-2 in Fig. 2b]. The change arises from the formation of O–H bonding during hydrogenation, supposing that the attachment of H^+ ion to oxygen lowers the energy of O-p bands (Fig. S4 in the Supplementary Information).

The orbital-resolved spectral functions clearly demonstrate an orbital-selective mechanism that induces a MIT, as shown in Fig. 3b–d. The spectral function $A(\omega)$ of the a_{1g}-like orbital (panel b) exhibits a gap resulting from the enhancement of the bonding-antibonding splitting by the Δ-potential from inter-site correlations. This mechanism corresponds to a correlation-assisted Peierls transition from dimerization, as discussed in VO_2[11,12].

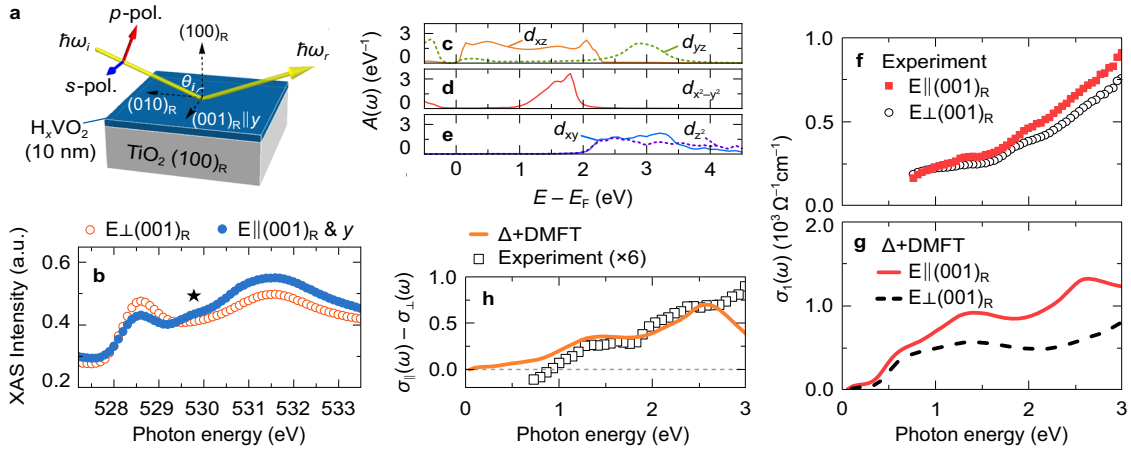

Fig. 4 Orbital-dependent optical properties of HVO_2. **a** Hydrogenated 10-nm-thickness VO_2/TiO_2 $(100)_R$ thin film and measurement geometry in XAS and ellipsometry. The $(001)_R$ direction is parallel to the *y*-axis defined for the calculations in Fig. 1b. **b** O *K*-edge XAS spectra with $E \parallel (001)_R$ (filled circles) and $E \perp (001)_R$ (empty circles) for HVO_2 taken at 250 K. **c**–**e** Decomposed $A(\omega)$ calculated for **c** d_{xz} and d_{yz}, **d** $d_{x^2-y^2}$, and **e** d_{xz} and d_{z^2} orbitals. The intensity for inequivalent V1 and V2 atoms, total 4 atoms in unit cell, are summed up. **f**, **g** Optical conductivity $\sigma_1(\omega)$ spectra from (**f**) experiment and (**g**) Δ+DMFT. **h** The deviation of $\sigma_1(\omega)$ in $E \parallel (001)_R$, $\sigma_\parallel(\omega)$, and $E \perp (001)_R$, $\sigma_\perp(\omega)$. The experimental spectrum in symbols is multiplied by 6. Pol., polarization.

The e_g^π-like orbitals exhibit an orbital ordering with the d_{xz} orbital shifted above the Fermi energy (panel c) and a Mott gap formed in the d_{yz} orbital (panel d), driven by local correlations. In essence, the pronounced difference in the hopping anisotropy between a_{1g}- and e_g^π orbitals leads to two distinct mechanisms: a correlation-assisted Peierls and Mott transition for a_{1g} and e_g^π orbitals, respectively, which we define as an orbital-selective Mott and Peierls transition.

We note that there is no qualitative difference between the inequivalent V1 and V2 sites defined in Fig. 1a. The major features of the orbital orderings without correlations (defined with non-magnetic Wannier Hamiltonian), such as bonding-antibonding splitting of $d_{x^2-y^2}$ orbitals and energy of d_{xz} orbital higher than d_{yz} orbitals are the same for both sites with the octahedral distortions and attached hydrogen ion. Given the non-interacting orbital structure with the bonding-antibonding splitting of $d_{x^2-y^2}$ orbitals and the energy difference between d_{xz}/d_{yz} orbitals, the Mott and Peierls and Mott transition occurring by the inclusion of the inter-site and on-site correlations enhances the orbital splitting. The resulting orbital splitting is much larger (in the order of *U*) than that from structural effects (<0.4 eV), and the enhanced splittings dominate the orbital structures. The orbital energies from the non-magnetic Wannier tight-binding Hamiltonian are discussed in Sec. VII in the Supplementary Information.

The calculated optical conductivity matches with the important characteristics of the spectral transfer observed in the experiment, which strongly supports the orbital selective phase transition in HVO_2. Figure 3e shows the experimental $\sigma_1(\omega)$ of the VO_2 extracted from thin film grown on an Al_2O_3 substrate before and after hydrogenation. The $\sigma_1(\omega)$ of VO_2 calculated by using Δ-potential to include inter-site correlations [Fig. 3f] is consistent with that calculated by CDMFT[43] and also with the experimental data; this supports the validity of employing a static intra-dimer Δ-potential in our approach. Moreover, we find that the calculated optical conductivity of HVO_2 from Δ+DMFT successfully reproduces the essential features such as the optical gap, suppression of the spectral weight, and the blue shift of the charge transfer peak about 1.5 eV coming from the down-shift of O-*p* states (for details see Fig. S4 in the Supplementary Information). These results provide a strong support to the Mott and Peierls insulating phase as the ground state of HVO_2.

Polarization-dependent optical responses

An interesting feature resulting from the orbital-selective Mott and Peierls transition is orbital ordering, by which polarization-dependent responses are expected. We employ two different measurements, polarization-dependent X-ray absorption and ellipsometry, to further confirm the proposed Mott-Peierls insulating phase. We prepare an additional set of VO_2 films of 10-nm thickness grown epitaxially on TiO_2 (100) substrate, which allows measuring the polarization-dependent responses[36].

To obtain the orbital-dependent responses using polarized light, alignment of the VO_2 on the substrate is crucial[37]. The VO_2 films epitaxially grown on Al_2O_3 have a significant advantage due to the large band gap (~7 eV), allowing for the optical measurements up to the visible/UV ranges, but the VO_2 films have domains oriented in different directions inhibiting the polarization-dependent experiments. In contrast, the VO_2 films grown in TiO_2 are oriented in either $(100)_R$ or $(001)_R$[36,37], making it possible to perform polarization-dependent measurements up to the visible ranges.

Figure 4a presents the measurement geometry where the *s*- and *p*-polarized light is mainly parallel and perpendicular to $(001)_R$ (or *y*-axis) in Fig. 1, respectively. We find that the linear dichroism of O *K*-edge (O $1s \rightarrow 2p$ transition) of VO_2 (Fig. S3) before hydrogenation is in good agreement with that of single crystal VO_2[44–46]. This shows that our film on TiO_2 is oriented well-enough to detect the dichroism signal.

The X-ray absorption of fully hydrogenated HVO_2 in Fig. 4b confirms the calculated orbital polarization of an orbital selective Mott and Peierls insulator. We define the case of an intensity of $E \parallel (001)_R$ greater (less) than $E \perp (001)_R$ as positive (negative) dichroism. There are three characteristic features in the XAS: (1) a peak at 528.5 eV with negative dichroism, (2) a small peak at 529.5 eV with positive dichroism (marked with a star), and (3) peak around 532 eV with positive dichroism. The dichroism can be understood from the orbital-projected spectral function of each *d*-orbitals summed over all V-atoms in the unit cell presented in Fig. 4c–e. The negative dichroism of (1) can be understood from the d_{xz}-derived states located right above the Fermi energy [Fig. 4c], which hybridize mainly with O-p_x/p_z orbitals and thus have large absorption for the polarization in the *xz* [$E \perp (001)_R$] plane. The feature of (2) is associated with the transition to the $d_{x^2-y^2}$-derived antibonding states [Fig. 4d] in which the $d_{x^2-y^2}$-p_y hybridization prefers the absorption of $E \parallel (001)R$ (parallel to *y*-axis

in Fig. 1b), resulting in overall positive dichroism and the peak position well matches with the transition energy to the antibonding $d_{x^2-y^2}$ state. We find the positive dichroism of (3) is common for both VO_2 and HVO_2, due to the similar e_g^σ orbital structures between them.

The polarization-dependent optical conductivity $\sigma_1(\omega)$ provides further evidence of the proposed orbital structures of HVO_2. In both experiment and calculation, we find that the difference in $\sigma_1(\omega)$ between $E \parallel (001)_R$ and $E \perp (001)_R$ gradually increases up to 3 eV [Fig. 4f, g). We note that $\sigma_1(\omega)$ above 3 eV becomes unreliable due to a strong TiO_2 signal and thus not shown. Below 1 eV, the optical response is contributed mainly from the transitions from occupied d_{yz} and $d_{x^2-y^2}$ states to unoccupied d_{xz} states, having small matrix elements and dichroism. Above 1 eV, the transitions between bonding and antibonding $d_{x^2-y^2}$ start to be significant, having large matrix elements for $E \parallel (001)_R$ compared with $E \perp (001)_R$. This, in turn, results in a significant increase of the dichroism [Fig. 4h] at around 2.5 eV corresponding to the bonding-antibonding splitting of $d_{x^2-y^2}$ bands. We find that the measured dichorism in the experiment is roughly 6 times smaller than in the calculation. This is partially from the magnitude of the experimental optical conductivity being about half of the calculated one, resulting in about 50% reduction of the dichroism signal. The non-ideal sample may be another reason, such as oxygen vacancies formation on the surface during annealing or the coexistence of other remnant phases (e.g., mixed domains). Overall, the consistent trend of the experimental and theoretical dichroism in the optical conductivity further supports the orbital structures resulting from a Mott and Peierls transition.

We note that the inter-site correlations included with the Δ+DMFT approach are crucial for predicting the correct orbital reconstructions across the MIT. To confirm the role of the inter-site correlations, we have additionally performed single-site DMFT calculations that neglect these nonlocal effects (see Fig. S6 in the Supplementary Information). In this case we find that the orbital ordering pattern is not consistent with the polarization-dependent XAS. Moreover, the optical conductivity and its polarization show marked differences around the low-frequency region (see Supplementary Information for further discussion).

Outlook and conclusion

Several properties of the MIT in H_xVO_2 need further investigation. For example, since two different mechanisms are involved in the MIT, it is an essential question whether the two transitions occur synchronously or asynchronously, and how the hydrogens percolate into the films. Unveiling the dynamics of the intermediate state can answer such questions. Theoretically, a temperature-dependent self-energy calculated for the O1 and O2 structures by DFT plus cellular DMFT methods including both a_{1g} and e_g^π orbitals could predict whether two transitions occur simultaneously. This would be an important future direction to pursue in the future. Experimentally, systematic temperature-dependent measurements of the orbital polarization by polarized X-ray absorption, dimerization by X-ray diffraction, and conductivity by transport or optical absorption measurements can be used. These experiments would allow investigating the orbital occupation, structural parameters, and band gap as the function of temperature. A key to achieving systematic results here is to maintain the hydrogen content at different temperatures, which is challenging because the x of the H_xVO_2 films changes at a different rate at different temperatures and chamber pressure. Therefore, systematic studies and surrounding hydrogen gas pressure conditions need to be preceded in H_xVO_2.

To conclude, we have investigated the electronic and optical properties of H_xVO_2 across the MIT occurring in the highly hydrogenated limit. Our main finding is that the insulating phase is induced in an orbital selective way, in which the a_{1g}-like orbital undergoes a correlation-assisted Peierls transition due to the relatively large dimer hopping, in a similar fashion as in pure VO_2. On the other hand, the e_g^π-like orbitals undergo a Mott-insulator transition after orbital ordering. We identify this scenario as an orbital-selective hybrid Mott and Peierls transition. The resulting orbital structure from the MIT is supported by polarization-dependent XAS and ellipsometry, showing energy-dependent dichroism, as well as Δ+DMFT calculations which successfully reproduce the experimental data. To the best of our knowledge, this is the first study uncovering the nature of the insulating phase under hydrogenation by providing solid evidence of orbital reconstructions across the MIT.

Our results provide a potential pathway to stabilize an insulating phase by combining Peierls and Mott physics coexisting in orbital space. This is in close analogy to the M2 phase in VO_2 having alternating antiferromagnetic and dimerized edge-sharing chains[47]. The present compound, HVO_2, is the first example of a compound displaying coexistence of Mott and Peierls behavior without spatial separation, differentiated only in orbital space. The proposed hybrid mechanism for a MIT provides a route for devising functionalities of correlated oxides from the two main aspects. The broken orbital symmetry with large energy separation in the presence of the two distinct ordering gives polarization-dependent responses varying with light frequencies and the lowered crystalline symmetry can be utilized for the optical control of the MIT by exciting the dimer oscillation allowed by the distinct V1 and V2 sites. Moreover, we expect that the transition temperature of the MIT could be controlled by the uniaxial strain along the chain direction. Utilizing hydrogenation, we expect to control the MIT with a small electric field, which could be achieved by tuning the hydrogen doping to the MIT boundary such that modulating the orbital occupation by small applied electric fields could induce the MIT.

METHODS

Sample preparation

We prepared 30-nm-thick VO_2 films epitaxially grown on the Al_2O_3 (0001) substrate, and 10-nm-thick VO_2 on the TiO_2 substrate $(100)_R$ and $(001)_R$ using pulsed laser deposition. The top surface of the films was then deposited with nano-sized Pt-islands to implement hydrogen spillover method as described in refs. [23,36,37].

Spectroscopic ellipsometry

For the optical conductivity measurements, we used spectroscopic ellipsometry (M-2000) and implemented fitting program (V-VASE) of J. A. Woollam Co. The hydrogenation was controlled on a hot plate (annealing $T \sim 400$ K) under the flow of H_2 (5%)/Ar (95%) in air. Each measurement was immediately followed by the XRD to characterize the lattice constant, from which we applied the linear relation between hydrogenation and lattice constants[18,23] to obtain doping content x.

To obtain the anisotropic optical conductivity, we scanned the VO_2/TiO_2 $(100)_R$ and the TiO_2 $(100)_R$ substrate twice for each sample, with s-polarized light parallel to $(010)_R$ and $(001)_R$ by rotating the film in 90° in-plane. After fitting the substrate with experimental data, we modeled the anisotropic film on the anisotropic substrate and fitted the optical conductivity with experimental film data. The photon energy ranges of the thin film spectra are limited by the band gap of the substrates, which is around 3 eV for TiO_2 and 7 eV for Al_2O_3 (see Fig. S4).

NEXAFS

NEXAFS data were obtained at the beamline 2A of Pohang Accelerator Laboratory (PAL). The incident angle [θ_i in Fig. 4a] was

about 67.5°. To compare the XAS data with different light polarization, a constant offset below 510 eV has been subtracted. The resulting dichroism signal of VO_2 at the V L_3-edge are consistent with previous reports[46,48].

DFT+DMFT calculations

We performed first-principles DFT calculations within the generalized gradient approximation (GGA) using the Vienna ab-initio simulation package[49,50]. We used the projector augmented wave method[51] and Perdew–Becke–Erzenhof parametrization[52] for the exchange-correlation functional. The experimental lattice parameters[18] have been used for the O1 and O2 structures in which the $8 \times 8 \times 16$ and $8 \times 8 \times 8k$-point grids are used, respectively. The energy cut-off of 500 eV is used. For the insulating O2 phase, the effective tight-binding Hamiltonian consisting of the V-*d*-derived frontier orbitals ($d_{x^2-y^2}, d_{xz}, d_{yz}$) is obtained for four V-sites of the primitive unit cell of HVO_2 using the Wannier90 package[53], based on the non-magnetic DFT-GGA calculation. To this Hamiltonian a local Coulomb interaction term is added with interaction parameters similar to those of the undoped parent compound with $U = 3.5$ eV and $J = 0.7$ eV and solved by Δ+DMFT method in which $d_{x^2-y^2}$ orbitals have been treated with static inter-site correlations Δ of −1.0 eV within the Hubbard dimer approximation (for detail see the Supplementary Information). For d_{xz} and d_{yz} orbitals, we have used a continuous-time quantum Monte-Carlo impurity solver in the hybridization expansion with a density–density form of the interaction as implemented in the ALPS package[54]. The optical conductivity is calculated by upfolding the band structures[43]. The spectral functions from DMFT are upfolded to the *p-d* energy window. The optical matrix elements are calculated in the energy range containing O-*p* and V-*d* bands by upfolding the band structure[43]. The matrix elements were evaluated using the real space position operators in the Wannier basis.

DATA AVAILABILITY

All relevant data that support the findings of this study are available from the corresponding author on request.

CODE AVAILABILITY

The codes used are VASP, ALPS, and Wannier90 (http://www.wannier.org). Additional scripts and modifications of the last are available from the corresponding author upon reasonable request.

Received: 7 February 2022; Accepted: 7 September 2022;
Published online: 23 September 2022

REFERENCES

1. Imada, M., Fujimori, A. & Tokura, Y. Metal-insulator transitions. *Rev. Mod. Phys.* **70**, 1039–1263 (1998).
2. Khomskii, D. I. *Transition Metal Compounds* (Cambridge University Press, 2009).
3. Shi, R. et al. Phase management in single-crystalline vanadium dioxide beams. *Nat. Commun.* **12**, 4214 (2021).
4. Budai, J. D. et al. Metallization of vanadium dioxide driven by large phonon entropy. *Nature* **515**, 535–539 (2014).
5. Zhou, Y. & Ramanathan, S. Mott memory and neuromorphic devices. *Proc. IEEE* **103**, 1289–1310 (2015).
6. Lee, S. et al. Anomalously low electronic thermal conductivity in metallic vanadium dioxide. *Science* **355**, 371–374 (2017).
7. Morin, F. J. Oxides which show a metal-to-insulator transition at the Neel temperature. *Phys. Rev. Lett.* **3**, 34–36 (1959).
8. Goodenough, J. B. The two components of the crystallographic transition in VO_2. *J. Solid State Chem.* **3**, 490–500 (1971).
9. Zylbersztejn, A. & Mott, N. F. Metal-insulator transition in vanadium dioxide. *Phys. Rev. B* **11**, 4383–4395 (1975).
10. Sommers, C. & Doniach, S. First principles calculation of the intra-atomic correlation energy in VO_2. *Solid State Commun.* **28**, 133–135 (1978).
11. Biermann, S., Poteryaev, A., Lichtenstein, A. I. & Georges, A. Dynamical singlets and correlation-assisted peierls transition in VO_2. *Phys. Rev. Lett.* **94**, 026404 (2005).
12. Tomczak, J. M., Aryasetiawan, F. & Biermann, S. Effective bandstructure in the insulating phase versus strong dynamical correlations in metallic VO_2. *Phys. Rev. B* **78**, 115103 (2008).
13. Li, Z. et al. Hydrogen treatment for superparamagnetic VO_2 nanowires with large room-temperature magnetoresistance. *Angew. Chem. Int. Ed.* **55**, 8018–8022 (2016).
14. Shi, R. et al. Axial modulation of metal-insulator phase transition of VO_2 nanowires by graded doping engineering for optically readable thermometers. *J. Phys. Chem. C* **121**, 24877–24885 (2017).
15. Andreev, V. N., Kapralova, V. M. & Klimov, V. A. Effect of hydrogenation on the metal-semiconductor phase transition in vanadium dioxide thin films. *Phys. Solid State* **49**, 2318–2322 (2007).
16. Wu, C. et al. Hydrogen-incorporation stabilization of metallic VO_2(R) phase to room temperature, displaying promising low-temperature thermoelectric effect. *J. Am. Chem. Soc.* **133**, 13798–13801 (2011).
17. Wei, J., Ji, H., Guo, W., Nevidomskyy, A. H. & Natelson, D. Hydrogen stabilization of metallic vanadium dioxide in single-crystal nanobeams. *Nat. Nanotechnol.* **7**, 357–362 (2012).
18. Filinchuk, Y. et al. In situ diffraction study of catalytic hydrogenation of VO_2: stable phases and origins of metallicity. *J. Am. Chem. Soc.* **136**, 8100–8109 (2014).
19. Ioffe, A. & Regel, A. Non-crystalline, amorphous and liquid electronic semiconductors. *Prog. Semiconductors* **4**, 237–291 (1960).
20. Mott, N. F. Conduction in non-crystalline systems IX. the minimum metallic conductivity. *Philos. Mag.* **26**, 1015–1026 (1972).
21. Hardy, W. J., Ji, H., Paik, H., Schlom, D. G. & Natelson, D. Mesoscopic quantum effects in a bad metal, hydrogen-doped vanadium dioxide. *J. Phys. Condens. Matter.* **29**, 185601 (2017).
22. Zhang, Z. et al. Evolution of metallicity in vanadium dioxide by creation of oxygen vacancies. *Phys. Rev. Appl.* **7**, 034008 (2017).
23. Yoon, H. et al. Reversible phase modulation and hydrogen storage in multivalent VO_2 epitaxial thin films. *Nat. Mat.* **15**, 1113–1119 (2016).
24. Chen, S. et al. Sequential insulator-metal-insulator phase transitions of VO_2 triggered by hydrogen doping. *Phys. Rev. B* **96**, 125130 (2017).
25. Dissanayake, M. & Chase, L. L. Optical properties of CrO_2 and MoO_2 from 0.2–6 eV. *Phys. Rev. B* **10**, 6872–6879 (1978).
26. Eyert, V. The metal-insulator transitions of VO_2: a band theoretical approach. *Ann. Phys.* **11**, 650–704 (2002).
27. Hiroi, Z. Structural instability of the rutile compounds and its relevance to the metal–insulator transition of VO_2. *Prog. Solid State Chem.* **43**, 47–69 (2015).
28. Oh, S. et al. Energy-efficient Mott activation neuron for full-hardware implementation of neural networks. *Nat. Nanotechnol.* **16**, 680–687 (2021).
29. Tang, K. et al. Millikelvin-resolved ambient thermography. *Sci. Adv.* **6**, abd8688 (2020).
30. Brahlek, M. et al. Opportunities in vanadium-based strongly correlated electron systems. *MRS Commun.* **7**, 27–52 (2017).
31. Kim, S. Y. et al. Spectroscopic studies on the metal-insulator transition mechanism in correlated materials. *Adv. Mater.* **30**, 1704777 (2018).
32. Wang, S. et al. Scalable thermochromic smart windows with passive radiative cooling regulation. *Science* **374**, 1501–1504 (2021).
33. Jo, M. et al. Gate-induced massive and reversible phase transition of VO_2 channels using solid-state proton electrolytes. *Adv. Funct. Mater.* **28**, 1802003 (2018).
34. Chen, S. et al. Gate-controlled VO_2 phase transition for high-performance smart windows. *Sci. Adv.* **5**, eaav6815 (2019).
35. Cui, Y., Shi, S., Chen, L., Luo, H. & Gao, Y. Hydrogen-doping induced reduction in the phase transition temperature of VO_2: a first-principles study. *Phys. Chem. Chem. Phys.* **17**, 20998–21004 (2015).
36. Yoon, H., Park, J., Choi, S.-Y., Lee, D. & Son, J. Facet-dependent phase control by band filling and anisotropic electron-lattice coupling in HVO_2 epitaxial films. *Adv. Electron. Mater.* **4**, 1800128 (2018).
37. Park, J., Yoon, H., Sim, H., Choi, S.-Y. & Son, J. Accelerated hydrogen diffusion and surface exchange by domain boundaries in epitaxial VO_2 thin films. *ACS Nano* **14**, 2533–2541 (2020).
38. Qazilbash, M. M. et al. Electrodynamics of the vanadium oxides VO_2 and V_2O_3. *Phys. Rev. B* **77**, 115121 (2008).
39. Tomczak, J. M. & Biermann, S. Optical properties of correlated materials—or why intelligent windows may look dirty. *Phys. Status Solidi B* **246**, 1996–2005 (2009).
40. Tomczak, J. M. & Biermann, S. Materials design using correlated oxides: optical properties of vanadium dioxide. *EPL* **86**, 37004 (2009).
41. Tomczak, J. M. & Biermann, S. Effective band structure of correlated materials: the case of VO_2. *J. Condens. Matter Phys.* **19**, 365206 (2007).

42. Chen, L. et al. Tuning the phase transition temperature, electrical and optical properties of VO_2 by oxygen nonstoichiometry: insights from first-principles calculations. *RSC Adv.* **6**, 73070–73082 (2016).
43. Tomczak, J. M. & Biermann, S. Optical properties of correlated materials: generalized Peierls approach and its application to VO_2. *Phys. Rev. B* **80**, 085117 (2009).
44. Abbate, M. et al. Soft-x-ray-absorption studies of the electronic-structure changes through the VO_2 phase transition. *Phys. Rev. B* **43**, 7263–7266 (1991).
45. Koethe, T. C. et al. Transfer of spectral weight and symmetry across the metal-insulator transition in VO_2. *Phys. Rev. Lett.* **97**, 116402 (2006).
46. Haverkort, M. W. et al. Orbital-assisted metal-insulator transition in VO_2. *Phys. Rev. Lett.* **95**, 196404 (2005).
47. Pouget, J. P. et al. Dimerization of a linear Heisenberg chain in the insulating phases of $V_{1-x}Cr_xO_2$. *Phys. Rev. B* **10**, 1801–1815 (1974).
48. Aetukuri, N. B. et al. Control of the metal insulator transition in vanadium dioxide by modifying orbital occupancy. *Nat. Phys.* **9**, 661–666 (2013).
49. Kresse, G. & Furthmuller, J. Efficient iterative schemes for ab initio total-energy calculations using a plane-wave basis set. *Phys. Rev. B* **54**, 11169–11186 (1996).
50. Kresse, G. & Joubert, D. From ultrasoft pseudopotentials to the projector augmented-wave method. *Phys. Rev. B* **59**, 1758–1775 (1999).
51. Blochl, P. E. Projector augmented-wave method. *Phys. Rev. B* **50**, 17953–17979 (1994).
52. Perdew, J. P., Burke, K. & Ernzerhof, M. Generalized gradient approximation made simple. *Phys. Rev. Lett.* **77**, 3865–3868 (1996).
53. Mostofi, A. A. et al. An updated version of wannier90: a tool for obtaining maximally-localised Wannier functions. *Comput. Phys. Commun.* **185**, 2309–2310 (2014).
54. Bauer, B. et al. The ALPS project release 2.0: open source software for strongly correlated systems. *J. Stat. Mech. Theory Exp.* **2011**, P05001 (2011).

ACKNOWLEDGEMENTS

We acknowledge insightful discussions with D. Khomskii, A. J. Millis, B. C. Park, and J. Tomczak. This work was supported by the Institute for Basic Science (IBS) in Korea (Grant No. IBS-R009-D1), a Consolidator Grant of the European Research Council (Project CorrelMat-617196), and IDRSI-GENCI (Orsay) under project number t2020091393. S.Y.P. was supported by the National Research Foundation of Korea (NRF) grant funded by the Korea government (MSIT) (No. 2021R1C1C1009494) and by Basic Science Research Program through the NRF funded by the Ministry of Education (No. 2021R1A6A1A03043957). H.Y. and J.S. were supported by the Basic Science Program through the NRF grant funded by the Ministry of Science and ICT (No. 2020R1A4A1018935). C.S. was supported by the National Research Foundation (NRF) funded by the Ministry of Science and ICT(2020R1C1C1008734). S.K. was supported by the Global Ph.D. Fellowship Program through the NRF funded by the Ministry of Education (No. 2015H1A2A1034943).

AUTHOR CONTRIBUTIONS

S.K., S.B., S.B., T.W.N., and S.Y.P. designed research. S.K., S.B., H.Y., W.K., C.S., J.S., and S.Y.P. performed research. S.K., S.B., S.B., T.W.N., and S.Y.P. wrote the paper with contributions from all the authors.

COMPETING INTERESTS

The authors declare no competing interests.

ADDITIONAL INFORMATION

Supplementary information The online version contains supplementary material available at https://doi.org/10.1038/s41535-022-00505-y.

Correspondence and requests for materials should be addressed to Tae Won Noh or Se Young Park.

Reprints and permission information is available at http://www.nature.com/reprints

Publisher's note Springer Nature remains neutral with regard to jurisdictional claims in published maps and institutional affiliations.